PHOTONICS Research

Universal spectral purification of ultrahigh-Q microresonators for ideal soliton microcombs

XIN ZHOU,^{1,2,†} JINCHENG LI,^{1,3,†} MIN WANG,^{1,2} YUECHEN LEI,^{1,2} YINKE CHENG,⁴ ZE WANG,⁴ ZHONGSHAN ZHANG,¹ ZHILIN LI,^{1,5} HAO ZHANG,⁶ ZHISONG XIAO,³ QI-FAN YANG,^{4,7,8} D AND BEI-BEI LI^{1,2,5,*} D

¹Beijing National Laboratory for Condensed Matter Physics, Institute of Physics, Chinese Academy of Sciences, Beijing 100190, China

Received 20 May 2025; revised 9 August 2025; accepted 22 August 2025; posted 25 August 2025 (Doc. ID 568361); published 31 October 2025

Soliton microcombs offer a compact means to generate equally spaced spectral lines via a delicate balance of Kerr nonlinearity and anomalous dispersion in nonlinear microresonators. However, the simultaneous excitation of multiple transverse mode families can disrupt soliton formation and degrade spectral uniformity. Here, we demonstrate universal spectral purification of microresonators with ultrahigh intrinsic Q factors exceeding 10^8 . An aluminum ring is deposited onto a silica microdisk to eliminate high-order transverse modes selectively by introducing additional losses. The resulting soliton microcombs exhibit an ideal sech² spectral envelope and enable continuous tuning of the soliton repetition frequency over a 300 kHz range without compromising phase noise performance. Our approach can be universally applied to integrated photonic platforms to reduce transverse modes crowding in high-Q resonators, facilitating the generation of broadband classical and quantum light with ideal performance. © 2025 Chinese Laser Press

https://doi.org/10.1364/PRJ.568361

1. INTRODUCTION

Optical frequency combs were originally demonstrated using mode-locked femtosecond lasers (e.g., Ti:sapphire or fiber lasers), which generated an evenly spaced, phase-coherent spectrum of lines [1]. Since their inception, miniaturization of comb generators has been recognized as a critical objective for extending their application beyond conventional laboratory settings. Approximately a decade ago, dissipative Kerr solitons, often termed soliton microcombs, were discovered in nonlinear microresonators via Kerr-induced parametric oscillation [2,3]. Soliton microcombs have since been applied in diverse laboratory applications, including low-noise microwave synthesis [4,5], optical atomic clocks [6–8], high-precision spectroscopy [9,10], and telecommunications [11,12].

At the core of microcomb technology lie high-quality-factor (high-Q) microresonators, which have been realized across a broad range of material platforms [13–15]. The threshold power for parametric oscillation is given by

$$P_{\rm th} \propto \frac{V_{\rm eff}}{Q^2},$$
 (1)

emphasizing the necessity of high optical Q factors for lowpower operation (here $V_{\rm eff}$ is the mode volume). In microresonators, the primary loss mechanism is often scattering at material interfaces. A common strategy to enhance Q is to increase the separation between the optical mode and these interfaces (with air or cladding materials) [16,17]. However, this approach inevitably enlarges the microresonator's cross section, thereby increasing the number of supported transverse modes. Consequently, avoided mode crossings [18,19] (AMXs) occur more frequently in such multimode resonators. AMXs are known to induce spectral anomalies commonly referred to as dispersive waves (DWs) on soliton spectra [20,21], which can even cause instabilities of soliton microcombs [22,23]. Although deliberately generated DWs have been exploited to suppress noise transduction from the pump laser to the soliton repetition frequency [21,24], their presence limits the continuous tuning range of repetition frequency and degrades the

²University of Chinese Academy of Sciences, Beijing 100049, China

³School of Physics, Beihang University, Beijing 100191, China

⁴State Key Laboratory for Mesoscopic Physics and Frontiers Science Center for Nano-optoelectronics, School of Physics, Peking University, Beijing 100871, China

⁵Songshan Lake Materials Laboratory, Dongguan 523808, China

⁶School of Space and Earth Sciences, Beihang University, Beijing 100191, China

⁷Collaborative Innovation Center of Extreme Optics, Shanxi University, Taiyuan 030006, China

⁸e-mail: leonardoyoung@pku.edu.cn

[†]These authors contributed equally to this work.

^{*}Corresponding author: libeibei@iphy.ac.cn

ultimate noise performance [25]. For non-integrated resonators, such as ${\rm MgF_2}$ crystal resonators and ${\rm SiO_2}$ rod resonators, AMX mitigation has been demonstrated through boundary-shape engineering techniques such as diamond turning [26,27] or laser reflow [28]. However, these approaches are incompatible with mass-produced microresonators and cannot be universally adapted to integrated microresonator systems. Previous strategies for mitigating AMXs in integrated microcavities have typically relied on narrowing the resonator's cross section, for example, by incorporating a tapered waveguide section within the microresonator [29–31]. Unfortunately, such geometric confinement engineering often causes significant degradation of the Q factor, making them less favorable for soliton microcomb generation.

In this work, we present a universal approach to reduce the transverse modal density in on-chip high-Q microresonators. By depositing a metal ring on a silica microdisk, we introduce additional loss that selectively attenuates high-order modes. This technique reduces the number of modes within a 25 GHz free spectral range (FSR) from over 30 to merely six, while still preserving an ultrahigh intrinsic Q exceeding 10^8 . As a result, we achieve DW-free soliton microcombs with repetition frequencies that can be continuously tuned over a 300 kHz range with consistent phase noise performance. This mode purification method is suitable for mass-produced microresonators and can be further extended to integrated microresonator systems, holding promise for enabling broadband classical and quantum light sources with ideal performance.

2. PRINCIPLE

Figure 1(a) illustrates the concept of the metal-modified microdisk. Finite-element simulations of the optical modes indicate that high-order modes experience significantly increased attenuation due to their stronger overlap with the lossy metal, whereas the fundamental mode remains largely unperturbed. In other words, the metal ring acts as a lossy filter that selectively dampens high-order modes, thereby spectrally purifying the microresonator while maintaining the high Q of the fundamental mode.

The dispersion diagrams in Fig. 1(b) present the calculated results and provide insight into how the metal ring suppresses AMXs. The integrated dispersion $D_{\rm int}(\mu)$ is defined as

$$D_{\text{int}}(\mu) = \omega_{\mu} - \omega_0 - D_1 \mu = \frac{1}{2} D_2 \mu^2 + \mathcal{O}(\mu^3),$$
 (2)

where $D_1/2\pi$ represents the FSR and $D_2/2\pi$ is the second-order dispersion, with high-order terms $\mathcal{O}(\mu^3)$ deemed negligible. The coupled-mode theory [18,32] was employed to examine the variation in AMX as the loss rate of the crossing mode increases. For clarity, only the fundamental mode (soliton mode) and high-order mode (crossing mode) families are considered here, with a coupling strength G. Thus, the eigenvalues of the hybrid modes are given by

$$\omega_{\mu\pm} = \bar{\omega} \pm \sqrt{\left[\frac{(\omega_{\mu,s} - \omega_{\mu,c}) + i(\gamma_s - \gamma_c)}{2}\right]^2 + G^2}, \quad (3)$$

where

$$\bar{\omega} = \frac{(\omega_{\mu,s} + \omega_{\mu,c}) + i(\gamma_s + \gamma_c)}{2},$$
 (4)

where $\omega_{\mu,s}$ and $\omega_{\mu,c}$ represent the unperturbed μ th resonant frequencies of the soliton and crossing modes, respectively, while $\gamma_s/2\pi$ and $\gamma_c/2\pi$ denote their corresponding loss rates.

Assuming that the two transverse modes are represented by orthogonal states ψ_s and ψ_c in the absence of coupling (G=0), the hybrid eigenstate under finite coupling $(G \neq 0)$ can be expressed as

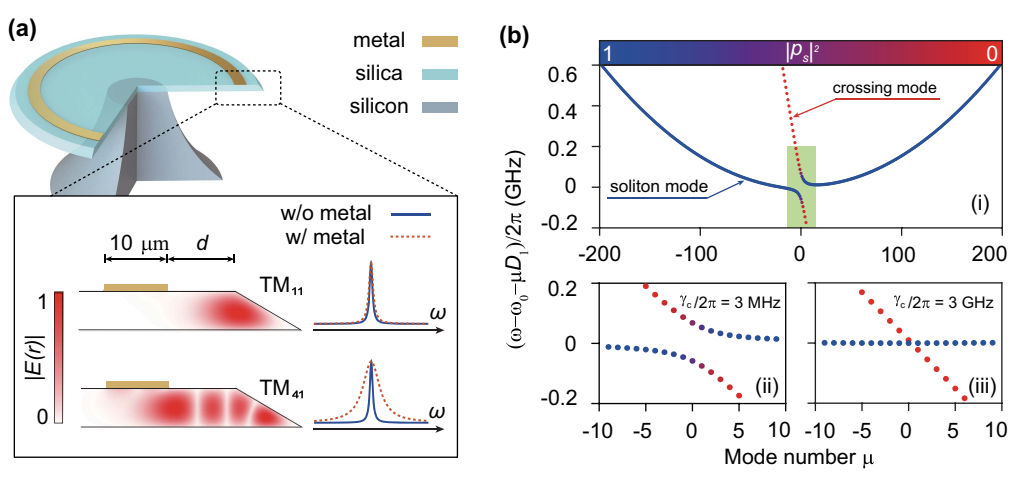


Fig. 1. Simulated characteristics of the metal-modified microdisk. (a) Schematic of a wedge-shaped silica microdisk with a top-mounted aluminum ring (proportions exaggerated for clarity). Inset: simulated optical field profiles of the fundamental and a high-order TM mode in the disk cross-section, along with their corresponding linewidths comparing cases with/without metal. The yellow regions denote the 10-µm-wide metal ring, and d is the gap between the metal ring and the upper edge of the 30° wedge. (b) Theoretical integrated dispersion of the hybrid modes formed by coupling between the fundamental mode (soliton mode) and a high-order mode (crossing mode), simulated for $\gamma_c/2\pi = 3$ MHz (i), (ii) and $\gamma_c/2\pi = 3$ GHz (iii). Panels (ii) and (iii) are zoomed-in views of the green shaded area in (i) around the AMX. The color scale represents the probability percentage of the soliton mode ($|p_s|^2$) within the respective hybrid mode. Other simulation parameters are: $\gamma_s/2\pi = 3$ MHz, $D_{1,s}/2\pi = 25.03$ GHz, $D_{2,s}/2\pi = 30.6$ kHz for the soliton mode; $D_{1,c}/2\pi = 25.00$ GHz, $D_{2,c}/2\pi = -66.0$ kHz for the crossing mode; and coupling strength $G/2\pi = 63$ MHz.

$$\Psi_{\mu\pm} = p_s \psi_s + p_c \psi_c, \tag{5}$$

with $\Psi_{\mu\pm}$ corresponding to the upper and lower branches in Fig. 1(b). The normalized probability amplitudes p_s and p_c are given by

$$\begin{pmatrix} p_s \\ p_c \end{pmatrix} = \frac{1}{N} \begin{pmatrix} \pm \sqrt{\alpha^2 + 1} + \alpha \\ 1 \end{pmatrix}, \tag{6}$$

where N is a normalization constant and

$$\alpha = \frac{(\omega_{\mu,s} - \omega_{\mu,c}) + i(\gamma_s - \gamma_c)}{2G}.$$
 (7)

The point color quantifies the fundamental mode fraction in the hybrid eigenvectors ($|p_s|^2$). In the absence of additional loss ($\gamma_c/2\pi=3$ MHz), by setting $G/2\pi=63$ MHz, the fundamental and crossing mode families strongly hybridize at their intersection, producing an AMX (indicated by the abrupt perturbation in the dispersion curve). In contrast, with a large loss introduced to the crossing mode ($\gamma_c/2\pi=3$ GHz), the mode hybridization is effectively eliminated, and the dispersion curve of the fundamental mode remains smooth and unperturbed through the crossing region. In other words, the metal ring acts as a dissipation engineering that selectively dampens high-order modes, thereby suppressing AMXs and spectrally purifying the microresonator while maintaining the high Q of the fundamental mode.

3. EXPERIMENTAL RESULTS

A. Device Fabrication

Figure 2(a) schematically depicts the key fabrication steps for the metal-modified microdisk. First, silica microdisks with a wedged edge were formed by photolithography and hydrofluoric (HF) wet etching of a 6- μ m-thick thermal SiO $_2$ layer on a silicon substrate. This process yielded microdisks with smooth wedges of $\sim\!30^\circ$. Next, the concentric metal ring pattern was transferred onto the microdisks via a second photolithography. Here, a full-ring metal along the circumference is used instead of a partial one to ensure optimal absorption efficiency and prevent backscattering induced by refractive index discontinuities. A 150-nm-thick Al layer was then deposited, followed by a 20-nm-thick aurum (Au) layer, using electron beam physical vapor deposition. The Al layer exhibited strong adhesion to silica and

a high absorption coefficient of 1.145×10^6 cm⁻¹ [33]. The Au layer acted as a protective coating to prevent oxidation of Al and maintained surface hydrophobicity to reduce surface roughness during the subsequent etching process [34]. After removal of excess metal through the lift-off process, structural release was accomplished through xenon difluoride (XeF₂) isotropic etching of the silicon pedestal to produce suspended microdisks with ~100 μ m undercut region. A scanning electron microscope (SEM) image of the fabricated device is shown in Fig. 2(b), including a close-up of the smooth wedge region of the microdisk with the deposited metal ring.

B. Device Characterization

To illustrate the effect of the metal ring on the mode spectrum, we measured the transmission and dispersion properties of the resonators under three representative conditions: (i) a bare microdisk (absence of metal), (ii) a metal-modified microdisk with a relatively distant ring ($d = 28.8 \mu m$), and (iii) a metal-modified microdisk with the optimal ring placement $(d = 14.8 \mu m)$. To ensure consistent coupling conditions, the cross-sectional diameter of the tapered fiber and its coupling position on the microdisk wedge were maintained throughout the measurements. Figure 3(a) shows examples of normalized transmission spectra spanning across three FSRs around 1550 nm under the TM polarization for each condition. These spectra indicate a dense set of resonances in case (i), and only a slight reduction in mode density for the device with the far-separated metal ring in case (ii). In contrast, the device with optimal distance in case (iii) shows far fewer resonances, consistent with many high-order modes being extinguished. We also extracted the integrated dispersion (D_{int}) curves for the resonances in each case, as plotted in Fig. 3(b). Approximately 400 resonances were identified across 1510-1590 nm, where the color of each data point corresponds to the on-resonance transmission depth. Consecutive groups of points correspond to distinct mode families, and the inset provides an enlarged view of the fundamental mode family. In the bare microdisk, numerous mode families appear within an FSR, and numerous AMXs are evident for the fundamental mode family. With the metal ring at $d = 28.8 \mu m$, the overall mode density is still high and an AMX is still present [orange dashed highlight in Fig. 3(b-ii)]. By comparison, for the

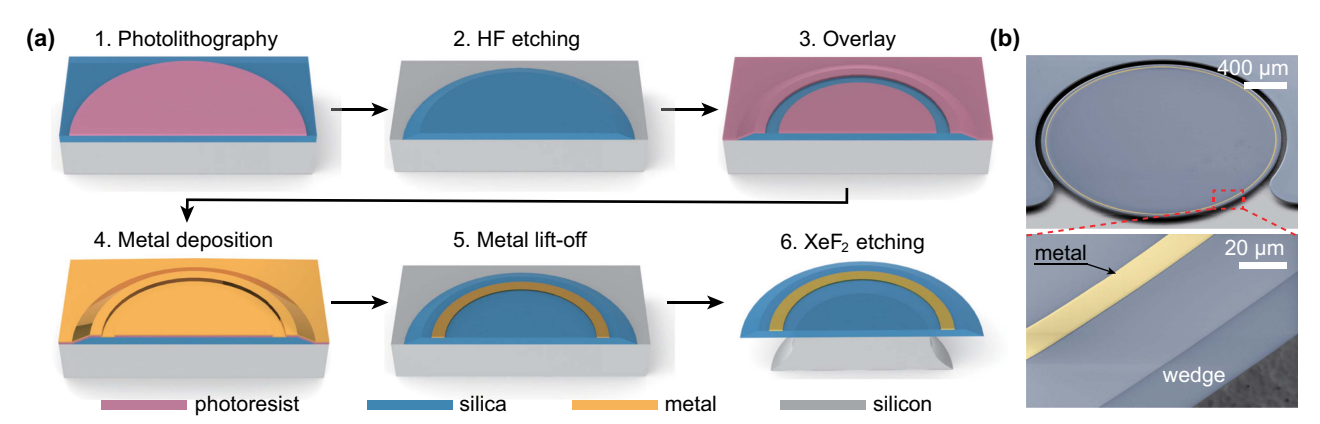


Fig. 2. Fabrication process of the metal-modified microdisk resonator. (a) Simplified fabrication process flow. (b) Top-view SEM image of a fabricated metal-modified resonator (top panel) and magnified view near the wedge (bottom panel).

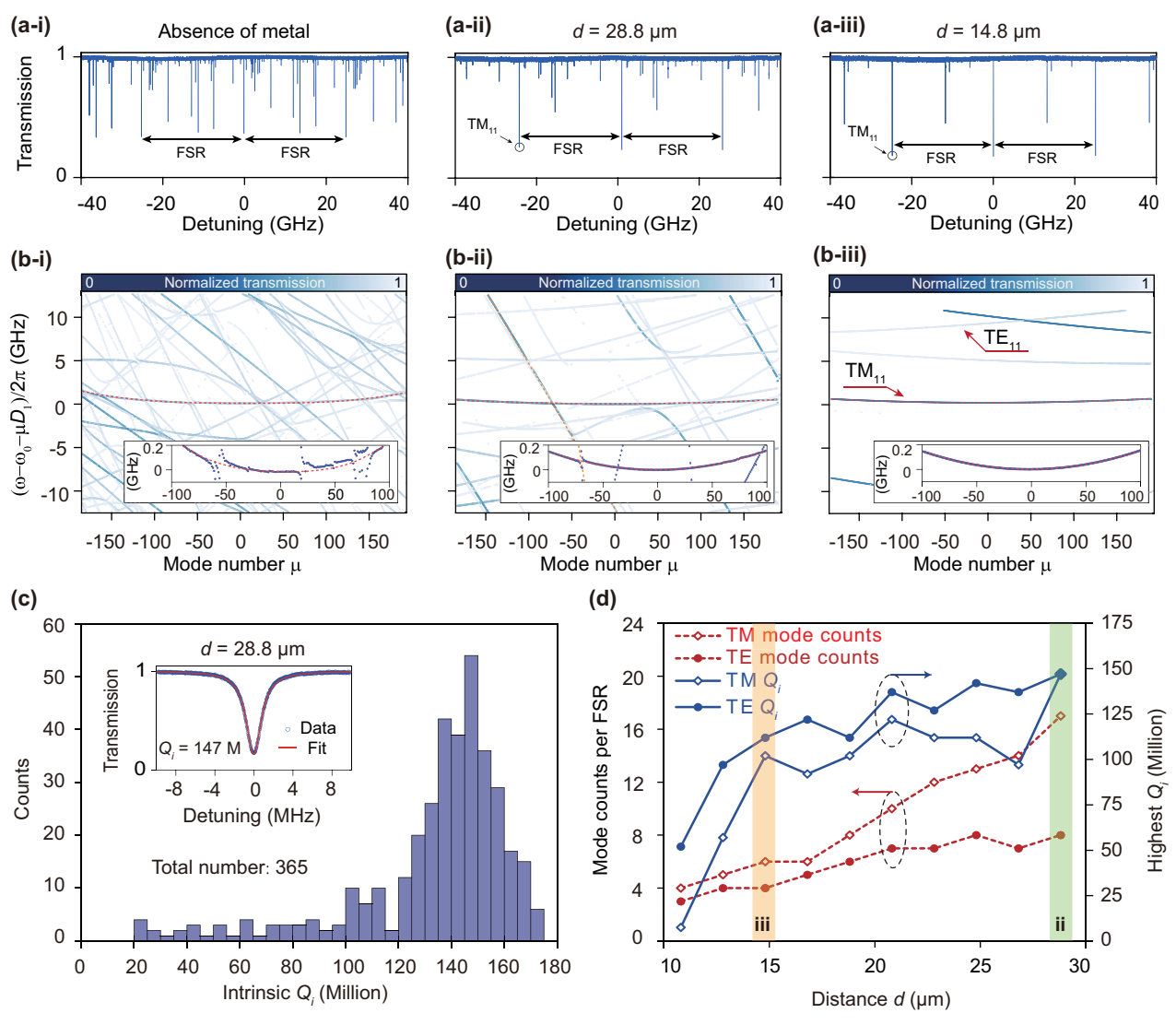


Fig. 3. Mode statistics. Three device geometries are evaluated: (i) bare microdisk (absence of metal), (ii) metal-modified microdisk with spacing $d=28.8~\mu m$, and (iii) metal-modified microdisk with spacing $d=14.8~\mu m$. (a) Normalized transmission spectra of the TM modes near 1550 nm. (b) Measured integrated dispersion of TM modes. Red and orange dashed lines indicate the soliton family and the corresponding high-order crossing mode family, respectively; insets show the enlarged window for mode index $\mu \in [-100,100]$. Point color encodes the mode-dip depth. (c) Histogram of intrinsic quality factors Q_i for 365 TM₁₁ modes between 1510 nm and 1590 nm at $d=28.8~\mu m$, with a most probable $Q_i \approx 1.47 \times 10^8$. Inset: example TM₁₁ mode (blue circles) and Lorentzian fit (red) yielding $Q_i = 1.47 \times 10^8$. (d) Number of modes per FSR (red) and the highest observed Q_i (blue) versus metal spacing d, for TE (dots) and TM (circles) families. Green and orange shadings correspond to cases (ii) and (iii), respectively.

optimized device at $d=14.8~\mu m$, both the number of modes and any measurable AMX perturbations are greatly reduced. The dispersion curve for the fundamental mode in case (iii) is essentially smooth and uninterrupted across the measurement range, confirming that the metal-induced loss is effectively filtering out the high-order mode that caused the AMXs in the other cases. Additionally, no AMX was observed between fundamental modes with different polarizations within a wide range of the laser wavelengths.

Moreover, from the wide spectral spanning over 80 nm, the highest intrinsic Q factor (Q_i) and mode density were also assessed as a function of the separation d. A statistical distribution of Q_i for the fundamental TM_{11} mode family is shown in Fig. 3(c) for case (ii), and the most probable Q_i is around

 1.47×10^8 , where the metal has only a minor impact on the Q factor of the fundamental mode at this distance. High-order transverse modes, on the other hand, experience increased loss due to the metal ring. As d is reduced, we observe that the Q of high-order modes drops while the fundamental-mode Q remains high. Figure 3(d) quantifies the distribution of mode counts within one FSR and the maximum intrinsic Q factors for different polarizations as a function of d. Note that the highest Q_i is derived from the fundamental mode family, which exhibits minimal overlap with the metal ring. The Q-factor distribution of the fundamental modes over a wide wavelength range is presented in Appendix B. Meanwhile, due to the wedge-induced non-orthogonality between TE and TM modes [35], the number of modes in different polarizations overlaps

partially. Figure 3(d) also reveals that TM modes experience more absorption losses from Al, due to their larger electric field intensity at the Al-SiO₂ interface. In our devices, an optimal spacing of $d=14.8~\mu m$ was identified: at this distance, the number of resonant modes within one FSR is reduced from >30 (in a bare disk) to only six, while the fundamental mode still retains an intrinsic Q exceeding 10^8 .

C. Soliton Microcomb Generation

Next, we investigated soliton microcomb generation in these devices. We employed the auxiliary-laser-assisted method to reliably access single-soliton states in the microdisk [36–38]. In our setup, the pump and auxiliary beams were derived from a single 1550 nm laser source. An ~8 MHz frequency offset was imposed between the two beams using acousto-optic modulators (AOMs), ensuring precise separation for thermal compensation. Both beams were coupled counter-propagating into the microdisk [28,39]. The auxiliary laser was blue-detuned relative to the pump laser to compensate for the abrupt thermal drift of the mode during the soliton generation and establish a thermally steady state.

Using this auxiliary-laser-assisted approach, we successfully generated single-soliton frequency combs in all three devices (i–iii). Upon soliton formation, the laser tuning was stopped, and the pump light was filtered out from the output. The soliton's repetition frequency $(f_{\rm rep})$ was monitored as a radio

frequency beat note using a fast photodiode, while its optical spectrum was recorded with an optical spectrum analyzer (OSA). The phase noise of the repetition rate was simultaneously measured with a phase noise analyzer (PNA) to assess comb stability. By maintaining the auxiliary laser blue-detuned on the soliton mode's thermally stable side and at a low enough power to prevent spurious nonlinear effects, we achieved stable soliton operation for hours without active feedback.

The optical spectra of the resulting combs are displayed in Fig. 4(a). In the bare microdisk (i) and the device with $d=28.8~\mu m$ (ii), the soliton spectra exhibit pronounced signatures of avoided mode crossings (AMXs), manifesting as additional spectral peaks superimposed on the ideal sech² envelope. These peaks correspond to DWs emitted due to the mode hybridization in AMXs [13]. In stark contrast, the spectrum from the spectrally purified resonator (iii) follows the expected sech² profile without parasitic spectral features, confirming that the soliton resides in a mode family free of significant AMXs over the entire comb bandwidth. This demonstrates that the DW observed in case (ii), associated with the AMX $\mu=75$ in Fig. 3(b) (orange dashed line), is fully suppressed in case (iii) due to our dissipation engineering.

The spectral width of the soliton optical frequency comb in Fig. 4(a-iii) is narrower than the former two cases due to the decreased $\,Q\,$ factor, with the explanations detailed in Appendix C below.

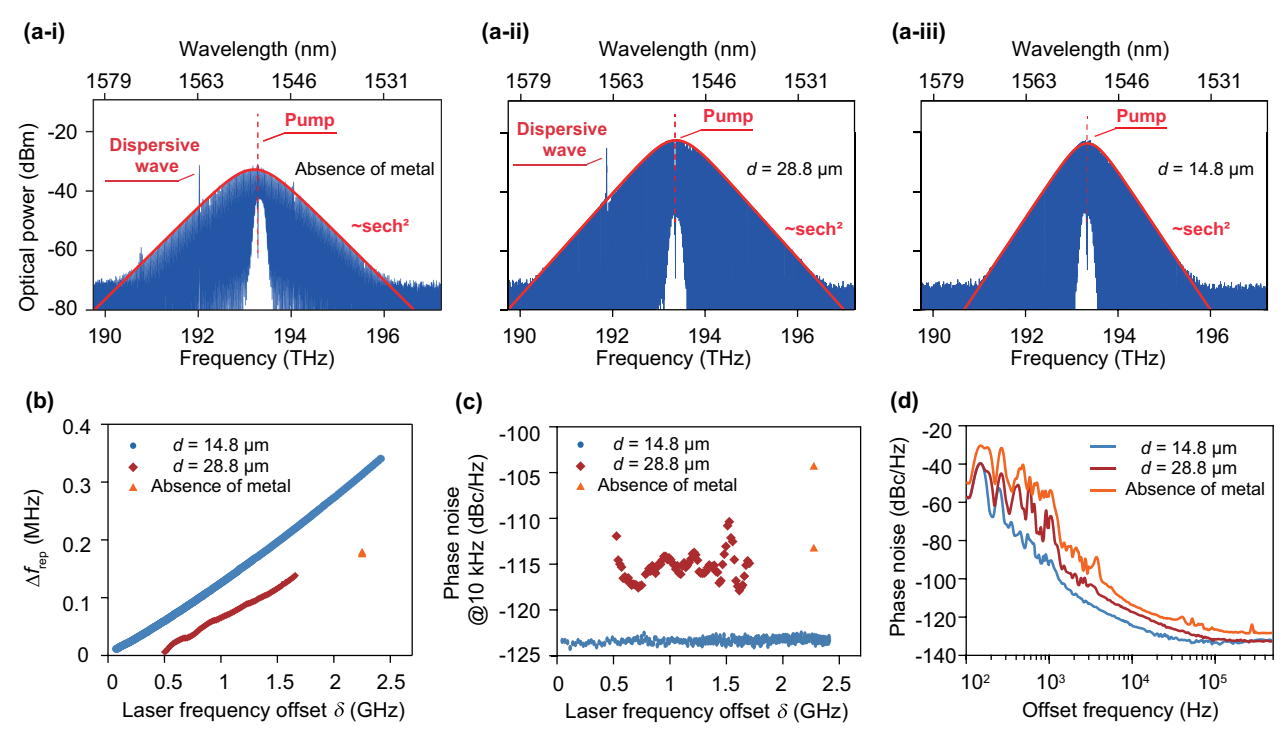


Fig. 4. Tunable and low-noise soliton microcomb generation in a spectrally purified microdisk. (a) Optical spectra of single-soliton combs (blue curves) with sech² fits (red curves) for the three resonator configurations. DWs are marked, showing pronounced AMXs-induced spectral features in (i) bare and (ii) weakly modified devices, contrasted with the ideal sech² profile in (iii) the spectrally purified case. (b) Repetition rate tuning: measured soliton f_{rep} (offset from 25.03 GHz) versus laser frequency detuning δ. In order to easily compare relative changes, different laser offset reference wavelengths are used in cases (i)–(iii), which are 1552.6 nm (i), 1551.59 nm (ii), 1551.7 nm (iii). (c) Phase noise dynamics: single-sideband phase noise (at 10 kHz offset) versus δ, highlighting the noise dependence on laser detuning. (d) Optimized phase noise: minimum achieved phase noise for each configuration.

D. Microwave Synthesis

The spectrally purified microresonator enables low-noise microwave synthesis with wide repetition rate tunability. We systematically characterized the soliton microcomb's repetition rate (f_{rep}) and phase noise evolution under pump laser frequency tuning for all three devices. In cases (ii) and (iii), the reduced mode density permits smooth laser frequency tuning in the soliton existence range without mode hops. In stark contrast, the high modal density of the bare microdiskhigh modal density of the bare microdisk in case (i) introduces unavoidable mode-hopping events during tuning, significantly degrading the soliton repetition tuning range. Figure 4(b) quantifies the soliton repetition rate's dependence on the laser frequency offset δ . As the pump laser is redshifted, f_{rep} redshifts continuously in cases (ii) and (iii), maintaining a single-soliton state. For the bare micordisk in case (i), mode-hopping disrupts this tuning process. Experimentally, we achieve continuous $f_{\rm rep}$ tuning over 300 kHz by redshifting the pump laser over 2.3 GHz.

Figure 4(c) tracks the phase noise at 10 kHz offset across different pump detunings δ . The spectrally purified resonator in case (iii) exhibits superior performance, with synthesized microwave maintaining ultralow phase noise (< -123 dBc/Hz) throughout tuning, illustrating robust comb coherence. This stability directly results from the spectrally purified resonator's

reduced mode density, which enables unimpeded thermal tuning without mode hops that plague conventional multimode microcavities [Fig. 4(b)]. Figure 4(d) shows the optimized single-sideband phase noise spectra for all three cases at ~25 GHz. The spectrally purified resonator in case (iii) can more easily achieve superior performance. Phase noise oscillations below 1 kHz originate from environmental perturbations (e.g., temperature and acoustic variations).

4. CONCLUSION AND OUTLOOK

Our strategy readily extends to integrated microring resonators [Fig. 5(a)]. Unlike previous methods that rely on geometric confinement for waveguide mode filtering, such as tapered ring widths [29] and partially etched structures [40], dissipation engineering enables spectrally purified whispering-gallery modes with inherently lower scattering losses and undisturbed dispersion characteristics of the fundamental mode, as it does not affect the structure of the fundamental mode.

As a concrete example, we consider an 800-nm-thick Si_3N_4 ring with a 100 GHz free spectral range. We model sidewall roughness as a thin absorptive layer whose loss rate matches typical Si_3N_4 scattering losses [41]. Two approaches are then compared: (i) confinement engineering by narrowing the waveguide width to suppress high-order transverse modes, and (ii)

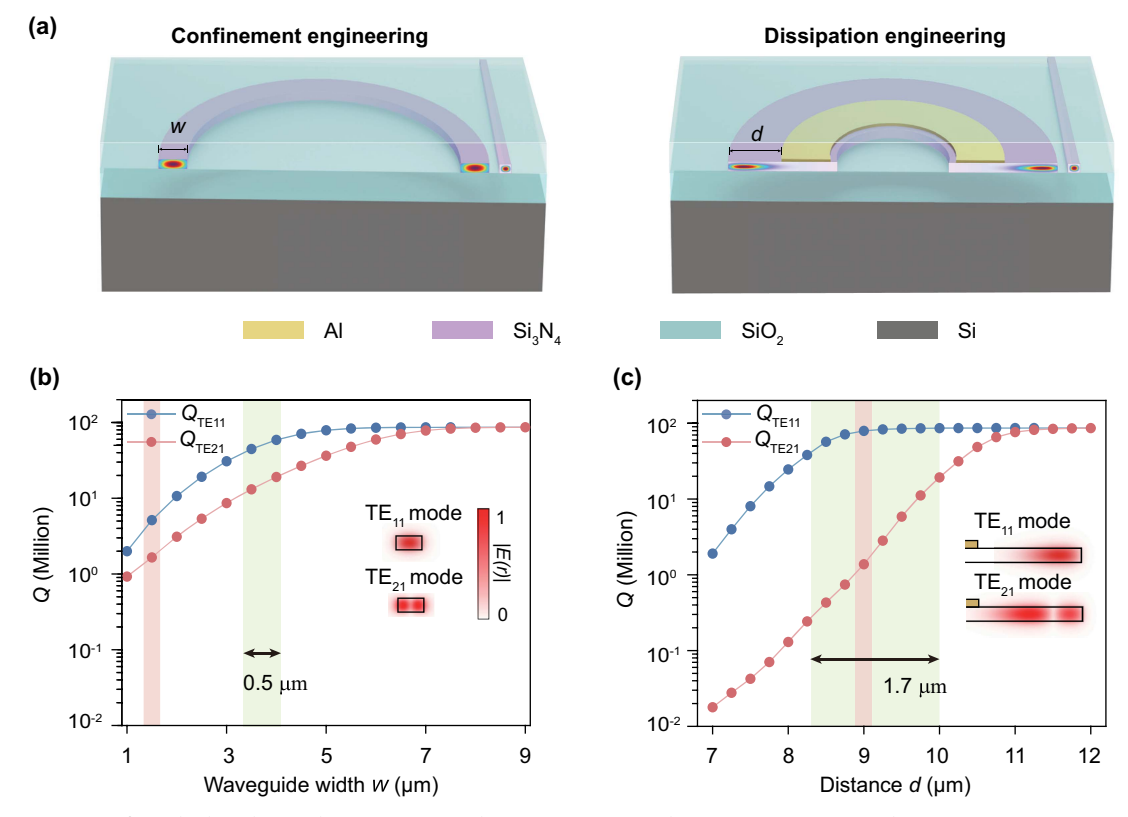


Fig. 5. Comparison of two high-order mode suppression techniques in integrated microresonators. (a) Schematic cross-sections (not to scale) of Si_3N_4 microring resonators for two approaches: confinement engineering (left) and dissipation engineering (right). The fundamental mode's optical field amplitude (color) is overlaid. (b) Simulated intrinsic Q of the fundamental mode TE_{11} (Q_{TE11} , blue) and second-order mode TE_{21} (Q_{TE21} , red) as a function of the microring waveguide width w (confinement engineering method). Inset: optical field profiles of the TE_{11} and TE_{21} modes as a function of the Al ring distance d from the microring edge (dissipation engineering method). Inset: optical field amplitudes for the TE_{11} and TE_{21} modes at d = 9 μm. The shaded red regions correspond to $Q_{TE21} = 1.5 \times 10^6$ and the green shaded regions correspond to the tolerance range, which is 0.5 μm and 1.7 μm for the two methods, respectively.

dissipation engineering by introducing a lossy metal ring to selectively attenuate them. In our finite-element simulations, the metal ring is assigned a loss rate far exceeding that of the side-wall layer. We extract intrinsic Q for the fundamental TE_{11} and higher-order TE_{21} modes and find that dissipation engineering drives Q_{TE21} down much faster than confinement engineering, as illustrated in Figs. 5(b) and 5(c). It is possible to realize Q_{TE21} at $\sim 1.5 \times 10^6$ while preserving Q_{TE11} at $\sim 7.9 \times 10^7$. This confirms that targeted loss can eliminate unwanted modes without compromising the fundamental-mode quality.

The tolerance range, was also analyzed for these two approaches, corresponding to the shaded green regions in Figs. 5(b) and 5(c), respectively. It is defined as the parameter range (w or d) that maintains $Q_{\rm TE11} > 43 \times 10^6$ (half the maximum $Q_{\rm TE11} = 86 \times 10^6$ in our simulation) and $\frac{Q_{\rm TE11}}{Q_{\rm TE21}} > 3$, corresponding to the requirements for high-Q and large suppression ratio of higher-order mode. The dissipation engineering method exhibits a wider tolerance range (1.7 μ m) than the confinement engineering method (0.5 μ m). A larger tolerance range reduces photolithography requirements in device fabrication and improves the device yield, thereby laying the foundation for mass production.

Maintaining few-mode operation at ultrahigh quality factors also unlocks both classical and quantum opportunities. Beyond serving as the low-noise backbone for microcomb-based RF oscillators, such resonators enable large-scale squeezed-state generation [42,43], with the absence of avoided-mode crossings preserving ideal multimode squeezing correlations. Our approach thus establishes a versatile platform for integrated photonics and fundamental quantum-optics research.

APPENDIX A: SIMULATION OF METAL-MODIFIED MICRODISK RESONATORS

Regarding the positional tolerance of the metal ring, we first simulate both mode counts with $Q>2\times 10^6$ and the Q factors of the fundamental mode family across different metal-to-wedge distances (d), as shown in red and blue curves, respectively, in Fig. 6. The results confirm that reducing the metal-to-wedge distance d gradually decreases Q factors of both the fundamental optical mode and higher-order optical modes. Therefore, the smaller d gives rise to fewer mode counts. As shown in Fig. 6, optimal mode filtering occurs within d=13–17 µm (pink region), where the mode count decreases significantly while the Q of the fundamental mode is maintained above 10^8 .

Experimentally, positional accuracy is ensured by the ultraviolet photolithography process, which can achieve an overlay error $<1~\mu\text{m},$ well within the tolerance range of the metal position.

APPENDIX B: CHARACTERIZATION OF METAL-MODIFIED MICRODISK RESONATORS

Figure 7 presents the measured wavelength-dependent *Q*-factor distributions of the fundamental TM and TE modes in both (i) bare silica microdisks and (ii)–(iv) metal-modified microdisks with varying metal-to-wedge distances (*d*). For the bare microdisk resonator, random occurrences of *Q*-factor

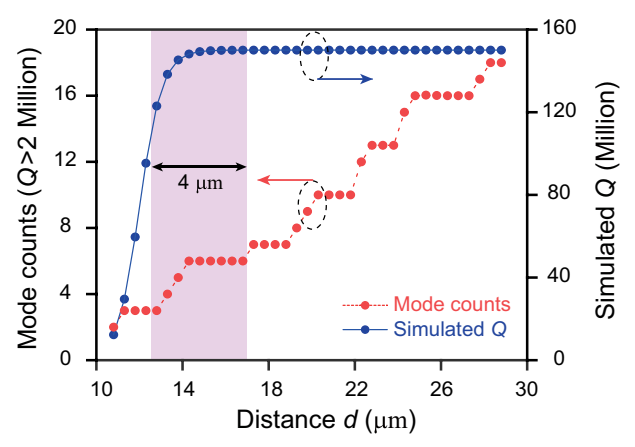


Fig. 6. Simulated mode counts and intrinsic Q of the microdisk. Simulated mode counts with Q>2 million in the metal-modified silica microdisks (red) and Q factors of the fundamental optical mode (blue) as a function of the metal-to-wedge distance d, with the pink region representing the metal positional tolerance range.

degradation across the entire scanning wavelength can be observed for both polarizations. However, in the metal-modified microdisks, such Q-factor degradation becomes localized within specific wavelength ranges, appearing as distinct dips in Figs. 7(a-ii)–7(a-iv). As the metal-to-wedge distance d decreases, the spectral range affected by Q-factor degradation gradually widens. However, this dip feature disappears for the TM-polarized modes in the metal-modified silica microdisk with $d=14.8~\mu \text{m}$ [Fig. 7(a-iv)], which can be explained via the interaction between the soliton mode and crossing mode. To explain this phenomenon more clearly and intuitively, we calculate the intrinsic Q-factor distribution of the hybrid modes formed by the coupling between the fundamental (soliton) mode and a high-order (crossing) mode using the coupled mode equations.

As shown in Fig. 7(c-i), when the Q factors for the soliton mode (Q_s) and crossing mode (Q_s) are comparable $(Q_s = 10^8,$ $Q_c = 5 \times 10^7$), the Q factors of the hybrid modes are approximately the average of their original Q factors, and the wavelength range within which the Q factors are affected is very localized. When the Q factor of the crossing mode decreases to $Q_c = 10^5$ [Fig. 7(c-ii)], it induces a reduction in the soliton mode's Q factor (Q_s) in a wider wavelength range, due to increased energy transfer to the crossing mode with a larger decay rate. However, as Q_c continues to decrease to 10^3 [Fig. 7(c-iii)], the crossing mode's contribution to the hybrid mode diminishes, and consequently the local decrease of Q_s can be suppressed by decreasing Q_c . This calculated result aligns well with our experimental measurements [Fig. 7(a)], where the Q factor of the crossing mode (typically higher-order mode) decreases as the d decreases. Notably, such a phenomenon is more pronounced for TM polarization compared to TE polarization modes, as shown in Figs. 7(a) and 7(b). This difference is believed to arise because TE modes exhibit weaker electric field intensity at the Al-SiO₂ interface, making them less sensitive to metal-induced loss than TM modes. Consequently, the crossing mode in TE polarization experiences insufficient damping

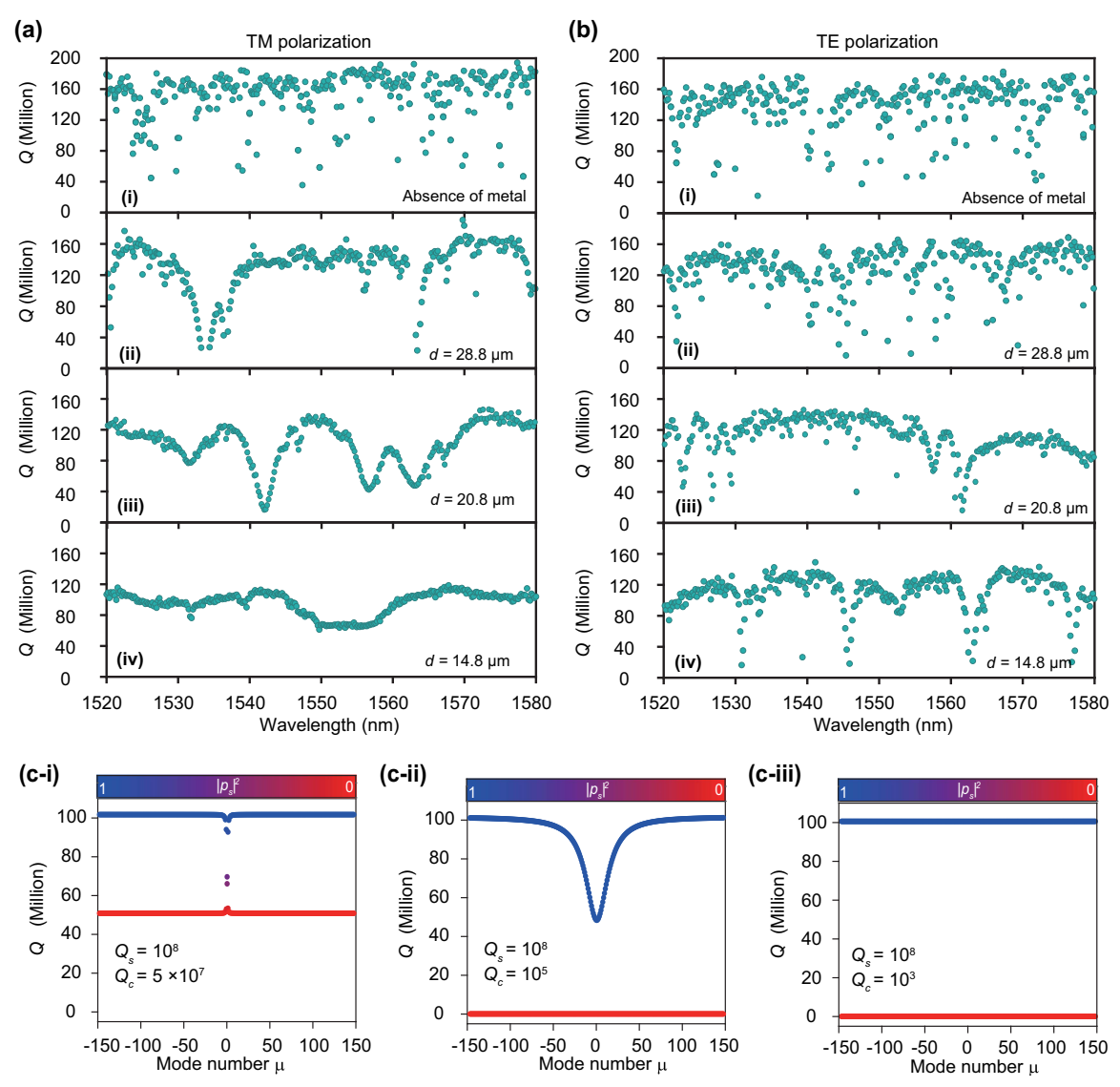


Fig. 7. Intrinsic *Q*-factor distributions in bare and metal-modified microdisks and simulated *Q*-factor distributions of the hybrid modes. Wavelength-dependent *Q*-factor distributions for the (a) TM- and (b) TE-polarized fundamental mode family of (i) bare silica microdisk and (ii)–(iv) metal-modified silica microdisks with $d = 28.8 \, \mu m$, $d = 20.8 \, \mu m$, and $d = 14.8 \, \mu m$, respectively. (c) Theoretical intrinsic *Q*-factor distributions of the hybrid modes formed by the coupling between the fundamental (soliton) mode and a high-order (crossing) mode, simulated for $Q_c = 5 \times 10^7$ (i), $Q_c = 10^5$ (ii), and $Q_c = 10^3$ (iii), while the soliton mode maintains $Q_s = 10^8$. The color bar represents the probability percentage of the soliton mode ($|p_s|^2$) within each hybrid mode.

to fully suppress the localized Q_s reduction, resulting in a distinguishable dip feature.

Additionally, as shown in Fig. 8, decreasing the metal-to-wedge distance (*d*) gradually reduces the mode-coupling-induced frequency shift between fundamental and high-order modes, indicating that the avoided mode crossings (AMXs) are not shifted out of the range of interest, but rather effectively suppressed.

APPENDIX C: EFFECT OF DISSIPATION ENGINEERING ON SILITON COMB

To balance thermal effects within the microcavity, we implemented an auxiliary laser method using the experimental setup

shown in Fig. 9. The pump and auxiliary lasers were generated from a single NKT laser (~1551 nm), which is driven by two acousto-optic modulators (AOMs), with a fixed frequency difference of ~8 MHz between them. The pump power for generating solitons is 100 mW, the effective mode area of the cavity is $A_{\rm eff}=36~\mu{\rm m}^2$, and the pump mode intrinsic Q is $Q_0=68$ million (metal-modified microcavity with $d=14.8~\mu{\rm m}$). When the pump laser reaches the soliton state at effective red detuning, the auxiliary laser resides in a thermally stable region on the blue-detuned side of the soliton mode. When the NKT laser wavelength is tuned, both the pump and auxiliary laser frequencies vary accordingly. As the NKT laser frequency decreases, the laser-tuning-induced thermal effect from the auxiliary laser redshifts the pump mode.

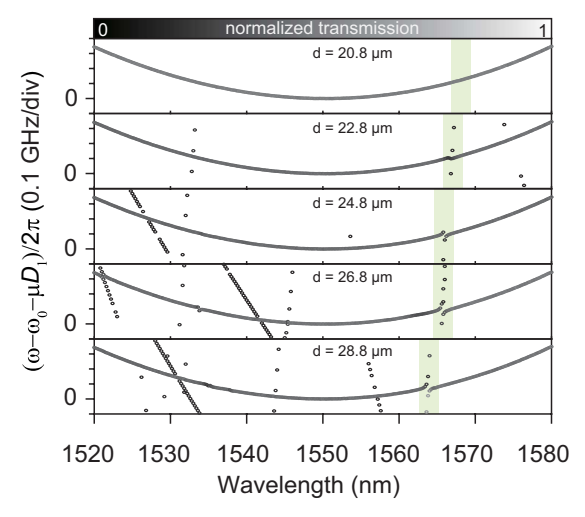


Fig. 8. Variation of AMX in metal-modified silica microdisks: integrated dispersion curves at different distances *d* under TM polarization, with the light green areas highlighting the location of the feature AMX.

Consequently, the pump mode redshifts in tandem with the pump light frequency. Additionally, after stabilizing to the soliton state, we carefully reduced the auxiliary laser power to 5–6 mW below the four-wave mixing threshold of $P_{\rm th}\approx 24.7$ mW for a cavity with d=14.8 µm ($P_{\rm th}\approx 7.7$ mW for a cavity with d=28.8 µm [13]). This prevents the auxiliary light from generating additional comb teeth along with increasing soliton repetition frequency noise.

The low mode density is a key reason why few-mode microcavities can achieve a 2.5 GHz pump tuning range without losing the soliton state. In high-mode-density cavities, the difference in optical field distribution between higher-order modes and the fundamental mode will lead to disparities in the average thermal optical field [25]. These disparities result in distinct thermal redshifts for different-order modes. Some higher-order modes may shift less than the pump mode during pump laser tuning, causing the soliton mode to cross higher-order modes. During this process, energy diversion to higher-order modes can trigger drastic local temperature changes, driving the soliton mode out of the soliton existence range (mode hopping). Reducing mode density can mitigate this mode-hopping effect by lowering the probability of encountering

higher-order modes during the pump tuning. Therefore, by combining the auxiliary laser's thermal stabilization effect with the advantages of low mode density of the metal-modified silica microdisk, we ultimately achieved a 2.5 GHz pump tuning range, which significantly exceeds the soliton existence range.

In Fig. 4(a-iii), the spectral width of the soliton comb is determined by the Q factor in our experiment, while the dispersion characterization remains consistent for microdisks with various metal-to-wedge distances d ($D_2/2\pi=30.1$ kHz for d=14.8 µm and $D_2/2\pi=30.6$ kHz for d=28.8 µm). The optical spectrum of the soliton, also a hyperbolic secant, is given by [2]

$$\Psi(\omega - \omega_p) = \sqrt{\frac{D_2}{2\kappa}} \cdot \operatorname{sech}\left(\frac{\omega - \omega_p}{\Delta\omega}\right),$$
 (C1)

where the maximum spectral width of the soliton, denoted as $\Delta\omega_{\rm max}$, is mathematically expressed by the formula

$$\Delta\omega_{\rm max} = 2 \cdot \sqrt{\frac{-\eta P_{\rm in} Q n_2}{\beta_2 n_0 V_{\rm eff}}} \propto \sqrt{\eta Q}.$$
 (C2)

Here, η is the coupling efficiency, defined as $\eta = \kappa_{\rm ext}/\kappa$, where $\kappa_{\rm ext}$ is the coupling rate between the microdisk and the tapered fiber and κ is the total cavity decay rate; $P_{\rm in}$ is the input pump power; Q is the quality factor of the soliton mode; n_2 is the nonlinear refractive index of the medium; β_2 is the group velocity dispersion; n_0 is the linear refractive index; $V_{\rm eff}$ is the effective mode volume. Thus, in our experiments, the other parameters remain the same, and the maximum width of the soliton spectrum $\Delta\omega_{\mathrm{max}}$ is only related to Q under critical coupling. Since the pump mode Q factor of the metalmodified microdisk with spacing $d=14.8~\mu\mathrm{m}$ and $d = 28.8 \ \mu \text{m}$ is $Q_{14.8} = 68 \times 10^6 \ \text{and} \ Q_{28.8} = 122 \times 10^6$, respectively, the theoretical ratio of their maximum soliton spectral width is $\sqrt{\frac{Q_{28.8}}{Q_{14.8}}}=1.34$, which is consistent with the experimental result $\sqrt{\frac{\Delta\omega_{28.8}}{\Delta\omega_{14.8}}}=1.35$ (here $\Delta\omega_{14.8}=$ 1.72 THz and $\Delta\omega_{28.8}=3.14$ THz represent the fitted spectral width of the soliton comb generated for $d = 14.8 \mu m$ and $d = 28.8 \mu m$).

Funding. National Natural Science Foundation of China (62222515, 12174438); Innovation Program for Quantum Science and Technology (2023ZD0301100); National Key

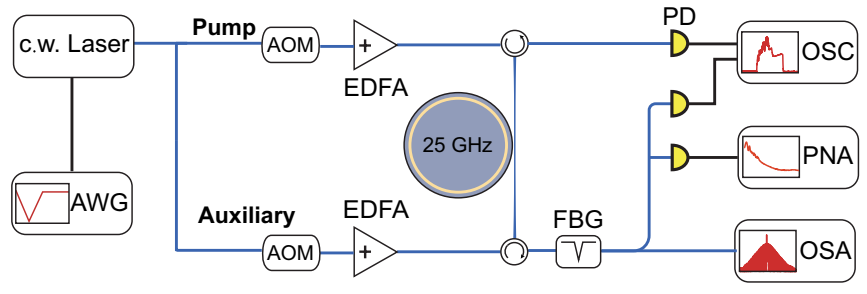


Fig. 9. Experimental setup for tunable low-phase-noise soliton microcomb with the metal-modified microdisk. Experimental setup for soliton microcomb generation with the auxiliary-laser-assisted method. AOM: acoustic-optic modulator; EDFA: Er-doped fiber amplifier; FBG: fiber Bragg grating; PD: photodiode detector; OSC: oscilloscope; PNA: phase noise analyzer; OSA: optical spectrum analyzer.

Research and Development Program of China (2021YFA1400700); Basic Frontier Science Research Program of Chinese Academy of Sciences (ZDBS-LY-JSC003); CAS Project for Young Scientists in Basic Research (YSBR-100).

Acknowledgment. This work was supported by the Synergetic Extreme Condition User Facility (SECUF, https://cstr.cn/31123.02. SECUF).

Disclosures. The authors declare no conflicts of interest.

Data Availability. Data underlying the results presented in this paper are available from the authors upon reasonable request.

REFERENCES

- S. A. Diddams, K. Vahala, and T. Udem, "Optical frequency combs: coherently uniting the electromagnetic spectrum," Science 369, eaay3676 (2020).
- 2. T. Herr, V. Brasch, J. D. Jost, et al., "Temporal solitons in optical microresonators," Nat. Photonics 8, 145–152 (2014).
- T. Herr, K. Hartinger, J. Riemensberger, et al., "Universal formation dynamics and noise of Kerr-frequency combs in microresonators," Nat. Photonics 6, 480–487 (2012).
- Kudelin, W. Groman, Q.-X. Ji, et al., "Photonic chip-based low-noise microwave oscillator," Nature 627, 534–539 (2024).
- S. Sun, B. Wang, K. Liu, et al., "Integrated optical frequency division for microwave and mmwave generation," Nature 627, 540–545 (2024).
- S. B. Papp, K. Beha, P. Del'Haye, et al., "Microresonator frequency comb optical clock," Optica 1, 10–14 (2014).
- T. E. Drake, T. C. Briles, J. R. Stone, et al., "Terahertz-rate Kerr-microresonator optical clockwork," Phys. Rev. X 9, 031023 (2019).
- K. Wu, N. P. O'Malley, S. Fatema, et al., "Vernier microcombs for integrated optical atomic clocks," Nat. Photonics 19, 400–406 (2025).
- M.-G. Suh, Q.-F. Yang, K. Y. Yang, et al., "Microresonator soliton dualcomb spectroscopy," Science 354, 600–603 (2016).
- E. Obrzud, M. Rainer, A. Harutyunyan, et al., "A microphotonic astrocomb," Nat. Photonics 13, 31–35 (2019).
- P. Marin-Palomo, J. N. Kemal, M. Karpov, et al., "Microresonator-based solitons for massively parallel coherent optical communications," Nature 546, 274–279 (2017).
- H. Shu, L. Chang, Y. Tao, et al., "Microcomb-driven silicon photonic systems." Nature 605, 457–463 (2022).
- X. Yi, Q.-F. Yang, K. Y. Yang, et al., "Soliton frequency comb at microwave rates in a high-Q silica microresonator," Optica 2, 1078–1085 (2015).
- Z. Ye, H. Jia, Z. Huang, et al., "Foundry manufacturing of tight-confinement, dispersion-engineered, ultralow-loss silicon nitride photonic integrated circuits," Photonics Res. 11, 558–568 (2023).
- R. Cheng, M. Yu, A. Shams-Ansari, et al., "Frequency comb generation via synchronous pumped χ⁽³⁾ resonator on thin-film lithium niobate," Nat. Commun. 15, 3921 (2024).
- H. Lee, T. Chen, J. Li, et al., "Chemically etched ultrahigh-Q wedgeresonator on a silicon chip," Nat. Photonics 6, 369–373 (2012).
- X. Ji, F. A. Barbosa, S. P. Roberts, et al., "Ultra-low-loss on-chip resonators with sub-milliwatt parametric oscillation threshold," Optica 4, 619–624 (2017).
- H. A. Haus and W. Huang, "Coupled-mode theory," Proc. IEEE 79, 1505–1518 (1991).
- Y. Liu, Y. Xuan, X. Xue, et al., "Investigation of mode coupling in normal-dispersion silicon nitride microresonators for Kerr frequency comb generation," Optica 1, 137–144 (2014).

- Q.-F. Yang, X. Yi, K. Y. Yang, et al., "Spatial-mode-interaction-induced dispersive waves and their active tuning in microresonators," Optica 3, 1132–1135 (2016).
- X. Yi, Q.-F. Yang, X. Zhang, et al., "Single-mode dispersive waves and soliton microcomb dynamics," Nat. Commun. 8, 14869 (2017).
- T. Herr, V. Brasch, J. Jost, et al., "Mode spectrum and temporal soliton formation in optical microresonators," Phys. Rev. Lett. 113, 123901 (2014).
- 23. H. Guo, E. Lucas, M. H. Pfeiffer, et al., "Intermode breather solitons in optical microresonators," Phys. Rev. X 7, 041055 (2017).
- A. C. Triscari, A. Tusnin, A. Tikan, et al., "Quiet point engineering for low-noise microwave generation with soliton microcombs," Commun. Phys. 6, 318 (2023).
- Q.-F. Yang, Q.-X. Ji, L. Wu, et al., "Dispersive-wave induced noise limits in miniature soliton microwave sources," Nat. Commun. 12, 1442 (2021).
- A. A. Savchenkov, I. S. Grudinin, A. B. Matsko, et al., "Morphology-dependent photonic circuit elements," Opt. Lett. 31, 1313–1315 (2006).
- 27. I. S. Grudinin and N. Yu, "Dispersion engineering of crystalline resonators via microstructuring," Optica 2, 221–224 (2015).
- W. Cui, X. Liu, H. Zhou, et al., "Ultra-low time jitter transform-limited dissipative Kerr soliton microcomb," Opt. Express 31, 37154–37161 (2023).
- A. Kordts, M. H. Pfeiffer, H. Guo, et al., "Higher order mode suppression in high-Q anomalous dispersion SiN microresonators for temporal dissipative Kerr soliton formation," Opt. Lett. 41, 452–455 (2016).
- S.-W. Huang, H. Liu, J. Yang, et al., "Smooth and flat phase-locked Kerr frequency comb generation by higher order mode suppression," Sci. Rep. 6, 26255 (2016).
- J. Nijem, A. Naiman, R. Zektzer, et al., "High-Q and high finesse silicon microring resonator," Opt. Express 32, 7896–7906 (2024).
- J. Wiersig, "Formation of long-lived, scarlike modes near avoided resonance crossings in optical microcavities," Phys. Rev. Lett. 97, 253901 (2006).
- K. M. McPeak, S. V. Jayanti, S. J. Kress, et al., "Plasmonic films can easily be better: rules and recipes," ACS Photonics 2, 326–333 (2015).
- K. Roodenko, M. Halls, Y. Gogte, et al., "Nature of hydrophilic aluminum fluoride and oxyaluminum fluoride surfaces resulting from XeF₂ treatment of Al and Al₂O₃," J. Phys. Chem. C 115, 21351–21357 (2011).
- 35. H. Wang, Y.-K. Lu, L. Wu, et al., "Dirac solitons in optical microresonators," Light Sci. Appl. 9, 205 (2020).
- H. Zhou, Y. Geng, W. Cui, et al., "Soliton bursts and deterministic dissipative Kerr soliton generation in auxiliary-assisted microcavities," Light Sci. Appl. 8, 50 (2019).
- S. Zhang, J. M. Silver, L. Del Bino, et al., "Sub-milliwatt-level microresonator solitons with extended access range using an auxiliary laser," Optica 6, 206–212 (2019).
- H. Zhang, L. Lu, J. Chen, et al., "Program-controlled single soliton generation driven by the thermal-compensated avoided mode crossing," J. Lightwave Technol. 41, 1801–1810 (2023).
- T. Wildi, V. Brasch, J. Liu, et al., "Thermally stable access to microresonator solitons via slow pump modulation," Opt. Lett. 44, 4447– 4450 (2019).
- 40. K. Y. Yang, D. Y. Oh, S. H. Lee, et al., "Bridging ultrahigh-Q devices and photonic circuits," Nat. Photonics 12, 297–302 (2018).
- J. Liu, G. Huang, R. N. Wang, et al., "High-yield, wafer-scale fabrication of ultralow-loss, dispersion-engineered silicon nitride photonic circuits," Nat. Commun. 12, 2236 (2021).
- 42. Z. Yang, M. Jahanbozorgi, D. Jeong, et al., "A squeezed quantum microcomb on a chip," Nat. Commun. 12, 4781 (2021).
- 43. Z. Wang, K. Li, Y. Wang, et al., "Large-scale cluster quantum microcombs," Light Sci. Appl. 14, 164 (2025).